

## Rapid Sampling of Severe Storms by the National Weather Radar Testbed Phased Array Radar

PAMELA L. HEINSELMAN, DAVID L. PRIEGNITZ, KEVIN L. MANROSS, TRAVIS M. SMITH, AND RICHARD W. ADAMS

*Cooperative Institute for Mesoscale Meteorological Studies, University of Oklahoma, and NOAA/OAR National Severe Storms Laboratory, Norman, Oklahoma*

(Manuscript received 14 September 2007, in final form 1 February 2008)

### ABSTRACT

A key advantage of the National Weather Radar Testbed Phased Array Radar (PAR) is the capability to adaptively scan storms at higher temporal resolution than is possible with the Weather Surveillance Radar-1988 Doppler (WSR-88D): 1 min or less versus 4.1 min, respectively. High temporal resolution volumetric radar data are a necessity for rapid identification and confirmation of weather phenomena that can develop within minutes. The purpose of this paper is to demonstrate the PAR's ability to collect rapid-scan volumetric data that provide more detailed depictions of quickly evolving storm structures than the WSR-88D. Scientific advantages of higher temporal resolution PAR data are examined for three convective storms that occurred during the spring and summer of 2006, including a reintensifying supercell, a microburst, and a hailstorm. The analysis of the reintensifying supercell (58-s updates) illustrates the capability to diagnose the detailed evolution of developing and/or intensifying areas of 1) low-altitude divergence and rotation and 2) rotation through the depth of the storm. The fuller sampling of the microburst's storm life cycle (34-s updates) depicts precursors to the strong surface outflow that are essentially indiscernible in the WSR-88D data. Furthermore, the 34-s scans provide a more precise sampling of peak outflow. The more frequent sampling of the hailstorm (26-s updates) illustrates the opportunity to analyze storm structures indicative of rapid intensification, the development of hail aloft, and the onset of the downdraft near the surface.

### 1. Introduction

The National Weather Radar Testbed Phased Array Radar (NWRTPAR; hereafter PAR) is a research radar that collects data from a 9.4-cm-wavelength, single-faced, phased-array antenna that supports adaptable scanning strategies and volumetrically scans storms at time scales of seconds instead of several minutes (Zrnić et al. 2007). Such high temporal resolution sampling provides an unprecedented opportunity to study rapidly evolving weather phenomena that are under-sampled temporally by conventional S-band radars like the Weather Surveillance Radar 1988-Doppler (WSR-88D). Given that the WSR-88D is approaching its 20-yr life span, and replacement with multifunction agile

beam PAR technology is an option under consideration (Weber et al. 2007; Zrnić et al. 2007), an initial investigation of the meteorological surveillance capabilities of the PAR is timely. For interested readers, a description of the concept of multifunction PAR, that is, simultaneous weather and aircraft surveillance, in light of the associated technological, operational, and cost issues, is given by Weber et al. (2007). Advantages of PAR for weather monitoring and improving data quality are examined by Zrnić et al. (2007).

This paper is the first detailed investigation of the capability of PAR, developed by the military for aircraft and missile surveillance, to provide high temporal resolution weather surveillance of severe storms. For comparison to conventional radars, this study explores how higher temporal resolution data from the PAR depicts storm evolution relative to the nearby Twin Lakes, Oklahoma, WSR-88D (KTLX) located about 20 km northeast of the PAR (Fig. 1). The comparative analysis of storm structure and evolution uses radar

---

*Corresponding author address:* Dr. Pamela L. Heinselman, 120 David L. Boren Blvd., Norman, OK 73072.  
E-mail: pam.heinselman@noaa.gov

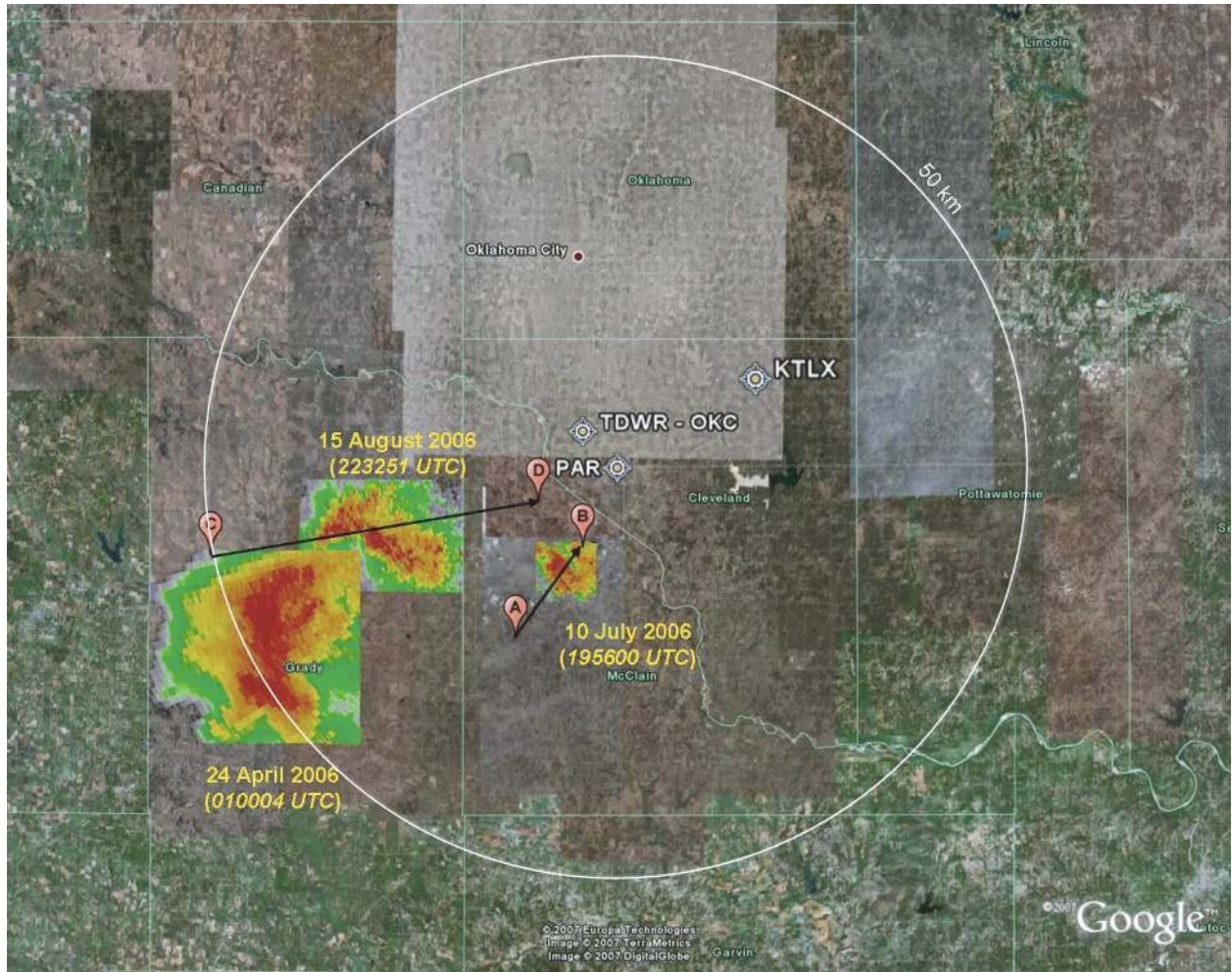


FIG. 1. Overview of the three storms studied in this paper. Radar reflectivity images ( $0.5^\circ$  elevation) are plotted relative to the PAR and are labeled according to the date of the particular event and the starting time of the image. The black arrows denote the direction and beginning and ending points of cross sections taken through the 10 Jul (A–B) and 15 Aug (C–D) 2006 storms (see section 3). Locations of the KTLX WSR-88D, Oklahoma City TDWR, and PAR radars are plotted and labeled. The range ring is 50 km from the PAR.

moments only to focus on scientific advantages of rapid scanning.

A description of the radar characteristics and capabilities of the PAR, relative to the WSR-88D, is given in section 2. The scientific implications of high temporal resolution PAR data are investigated in section 3 by performing a comparative analysis of storm structure and evolution for three convective storms that occurred during the spring and summer of 2006, including a re-intensifying supercell (24 April), a microburst (10 July), and a hailstorm (15 August; Fig. 1). In the one case where KTLX data are unavailable (15 August 2006), the discussion assesses gaps in the storm life cycle that would result from using the WSR-88D's volume coverage pattern 11 (VCP 11). Section 4 summarizes the

findings and speculates on potential operational advantages of PAR.

## 2. Comparison of PAR and WSR-88D

The most significant difference between the PAR and the WSR-88D is the antenna design. Zrníć et al. (2007) provide a detailed description of the PAR. The phased-array antenna forms a beam electronically by controlling the phases of 4352 transmit–receive elements, whereas the WSR-88D's beam is formed from a parabolic antenna. Additionally, in a WSR-88D, the steering of the beam is accomplished mechanically by rotating the antenna. Long volumetric updates generated by a rotating antenna can deliver spatially incongruous vertical storm structures and reduced data qual-

ity (smearing) due to antenna motion. In contrast, with a phased-array antenna, steering of the beam is done electronically by fixing the beam in a set direction while data are collected along a radial, and then instantly switching the beam to a new direction.

Currently, the PAR is a single-faced phased-array system that can scan a  $90^\circ$  sector while stationary. The PAR performs a VCP 12 scanning strategy (Brown et al. 2005) within 58 s rather than 258 s ( $90^\circ$  sector versus  $360^\circ$  sector, respectively), for example. The reduction in time required for volumetric updates produces a more realistic evolution of storm structures and eliminates smearing of the beam due to rotation of the antenna during data collection. An operational PAR configuration, however, would have a system containing four independent faces capable of scanning a complete  $360^\circ$  sweep. In essence, a four-faced PAR is like having four radars in one location, each scanning its own  $90^\circ$  sector. An important goal of an operational PAR system would be to match or exceed the current operational standards.

Worth noting is the unique potential of the phased-array antenna to make cross-beam wind, shear, and turbulence measurements (Zhang and Doviak 2007). Because the PAR has the capability of receiving signals from separate areas of its array of elements, cross-correlation analysis of signals from different directions is possible. This interferometric measurement capability allows angular shear and turbulence to be simultaneously measured along the transmitting beam (Zhang and Doviak 2007). Furthermore, if wind is uniform across the beam, crossbeam wind can be simultaneously measured with the along-beam (i.e., Doppler) component.

The PAR and WSR-88D antennas share three similarities: wavelength (S band: 9.4 cm versus 10 cm, respectively), range resolution (both 250 m), and the PAR can mimic WSR-88D VCP tilts and collect data at similar pulse repetition intervals. However, due to PAR hardware limitations [e.g., sensitivity to the number pulse repetition time (PRT) changes], standard batch cuts, that is, interlaced equivalent reflectivity (hereafter, reflectivity) and Doppler velocity scans, could not be used between  $1.8^\circ$  and  $6.4^\circ$ . To reduce the number of PRT changes, surveillance and Doppler pulses were grouped into  $18^\circ$  sectors. Hence, at these elevation angles, more time elapses (0.5 s or less) between the azimuthal reflectivity and velocity samples at a given beam position.

Owing to the different antenna designs, the PAR is dissimilar to the WSR-88D in several ways. First, electronic steering of the beam supports adaptable scanning of weather echo. Hence, the dwell time may be opti-

TABLE 1. Standard deviation values of reflectivity and velocity fields for employed VCPs.

Date; VCP	Moment	Std dev
24 Apr 2006; VCP 12	Reflectivity	1.05 dBZ
	Velocity	$0.95 \text{ m s}^{-1}$
10 Jul 2006; beam multiplexing VCP 12	Reflectivity	1.61 dBZ
	Velocity	$1.46 \text{ m s}^{-1}$
15 Aug 2006; high vertical resolution VCP	Reflectivity	1.90 dBZ
	Velocity	$1.87 \text{ m s}^{-1}$

mized to the temporal and spatial scales of a particular weather phenomenon and its distance from the radar. Furthermore, close to the radar ( $<35 \text{ km}$ ), where conventional VCPs may undershoot storm-top height, higher elevations may be easily added to a scanning strategy. The flexibility to sample storms with nontraditional scanning strategies provides the opportunity to explore trade-offs between accuracy and high-resolution temporal and spatial sampling. Accuracy requirements for WSR-88D scanning strategies are standard deviation values of 1 dBZ for reflectivity and  $1 \text{ m s}^{-1}$  for velocity for specific signal-to-noise ratios and standard deviations in the estimate of spectrum-width values (ROC 2007). In this study, theoretical computations of reflectivity and velocity standard deviation values (Doviak and Zrnić 1993) vary depending on the scanning strategy employed (Table 1). The WSR-88D accuracy requirements are met by the VCP 12 scanning strategy used to sample the 24 April 2006 supercell (section 3a). The scanning strategy used to sample the 15 August hailstorm has the lowest accuracy (1.90 dBZ and  $1.87 \text{ m s}^{-1}$ ); in this case accuracy was traded off for higher-resolution sampling in the vertical (41 tilts versus 14) and higher temporal sampling (26 s versus 5 min; section 3c). These differences in accuracy did not interfere with this study's goal to investigate the rapid evolution of severe storm structures.

Second, the PAR was developed with vertically polarized electromagnetic waves to track military missiles and airplanes, rather than to detect weather echo. Since a raindrop becomes flatter with increasing size, the magnitude of the reflectivity data diminishes compared to data collected with a horizontally polarized beam. Third, the beamwidth varies with azimuth. In the direction perpendicular to the antenna face, the beamwidth is  $1.5^\circ$ , which is quite similar to the effective beamwidth of the WSR-88D. When the beam is  $45^\circ$  from the perpendicular, the beamwidth is  $2.1^\circ$ . During data collection,  $1^\circ$  azimuthal sampling was used to provide finer resolution of the increasingly degraded data toward the edges of the sector scan.

Other data quality issues impacting the dataset are

ground clutter, second-trip echo, and sidelobe contamination (e.g., section 3c). Although the PAR's wider beamwidth makes the radar more susceptible to ground clutter than the WSR-88D or the Terminal Doppler Weather Radar (TDWR), in the near future this issue will be largely mitigated via clutter filtering software. Range and velocity ambiguity mitigation software is also under development to diminish second-trip echo and velocity aliasing issues. Although these data quality issues can be problematic, they did not interfere overwhelmingly with this study's goal of investigating the rapid evolution of severe storm structures.

### 3. Analysis of higher temporal resolution PAR data

This section investigates the scientific advantages of high temporal resolution PAR data by comparing data collected by the PAR and KTLX for two cases and approximating what the advantages would be in the third case. As mentioned in the introduction, the storms studied include a reintensifying supercell, a microburst, and a hailstorm that occurred in the spring and summer of 2006. Also described are the scanning strategies employed by the PAR during each data collection. (Animations that illustrate the differences in storm evolution sampled by the PAR and KTLX are available as supplemental material at the Journals Online Web site: <http://dx.doi.org/10.1175/2008WAF2007071.s1>.)

#### a. Reintensifying supercell

On 24 April 2006, conditions were favorable for supercell development near central Oklahoma. Surface dewpoint temperatures throughout the day remained at or near 20°C, whereas surface temperatures late in the day had risen to 27°C ahead of a cold front that had entered northwest Oklahoma. The surface-based convective available potential energy (CAPE) from the 25 April 0000 UTC Norman, Oklahoma, sounding was nearly 2500 J kg<sup>-1</sup> with 0–6-km shear of nearly 20 m s<sup>-1</sup> (not shown). Due to localized backing of the surface winds ahead of the cold front, 0–6-km shear ahead of the developing thunderstorms reached 23 m s<sup>-1</sup>.

On this day a line of supercell thunderstorms developed southwest of the PAR that was sampled continuously between 2000 UTC 24 April and 0300 UTC 25 April. Using a volume scan sampling rate of 58 s, a detailed evolution of the storm was captured by the PAR. None of these supercells produced a confirmed tornado. The storm of interest initially exhibited low-altitude convergence that developed into low-altitude cyclonic rotation (between 0050 and 0059 UTC 25 April). Meanwhile, a persistent mesocyclone in the midlevels of the storm strengthened and descended.

This event provides a unique comparison between PAR and KTLX since both radars scanned the same storms in southwest Oklahoma using similar scanning strategies (VCP 12).

#### 1) PAR SCANNING STRATEGY

The PAR employed a scanning strategy that mimicked the WSR-88D VCP 12 (Brown et al. 2005). Since more than one supercell occurred on this day, a 90° sector was chosen to maximize coverage, resulting in detailed 58-s volumetric updates. During the analysis period, the phased-array antenna was aimed toward the southwest of the radar to collect continuous data on the supercells that developed ahead of the dryline as they moved northeastward. Later the antenna was rotated to a more southerly bearing to follow the remaining storms as they decayed after sunset.

#### 2) ANALYSIS

The characteristics of the 0.5° elevation radar reflectivity and velocity fields are analyzed for a reintensifying supercell storm located within 60 km to the southwest of the PAR (Fig. 1). During the period of approximately one WSR-88D VCP 12 volume scan (0055:15–0059:28 UTC), the supercell undergoes significant evolution (Fig. 2). The north-northeastward movement of thunderstorm outflow (produced by the rear-flank downdraft) toward the storm-relative inflow creates an area of developing low-altitude convergence (Figs. 2b–d and 3) and cyclonic rotation (Figs. 2e,f and 3) located approximately 50 km southwest of the PAR (~70 km southwest of KTLX; Fig. 1). While the low-altitude convergence in the storm at 0055 UTC is not particularly strong (approximately  $-0.005$  s<sup>-1</sup>), it slowly increases in magnitude and area. Since significant increases in low-altitude convergence often precede rapid increases in low-altitude vorticity couplets and tornado development (Burgess and Magsig 1993, 1998; Burgess 2004), the capability to diagnose these types of trends in the base velocity fields is of interest to both the research and operational communities. The PAR's faster volume scan updates also depict the onset of divergent outflow produced by the forward-flank downdraft earlier than the WSR-88D (Figs. 2e and 3). Another impact of rapid volume scan updates is the ability to better view the inflow of air into the storms forward flank (Figs. 2e–h and 3; near-zero velocities east-northeast of the contracting and strengthening convergence signature).

Figure 4 illustrates PAR's enhanced ability to produce more timely updates of rotational characteristics within the storm. To clearly identify areas of significant rotation in a storm, azimuthal linear least squares de-

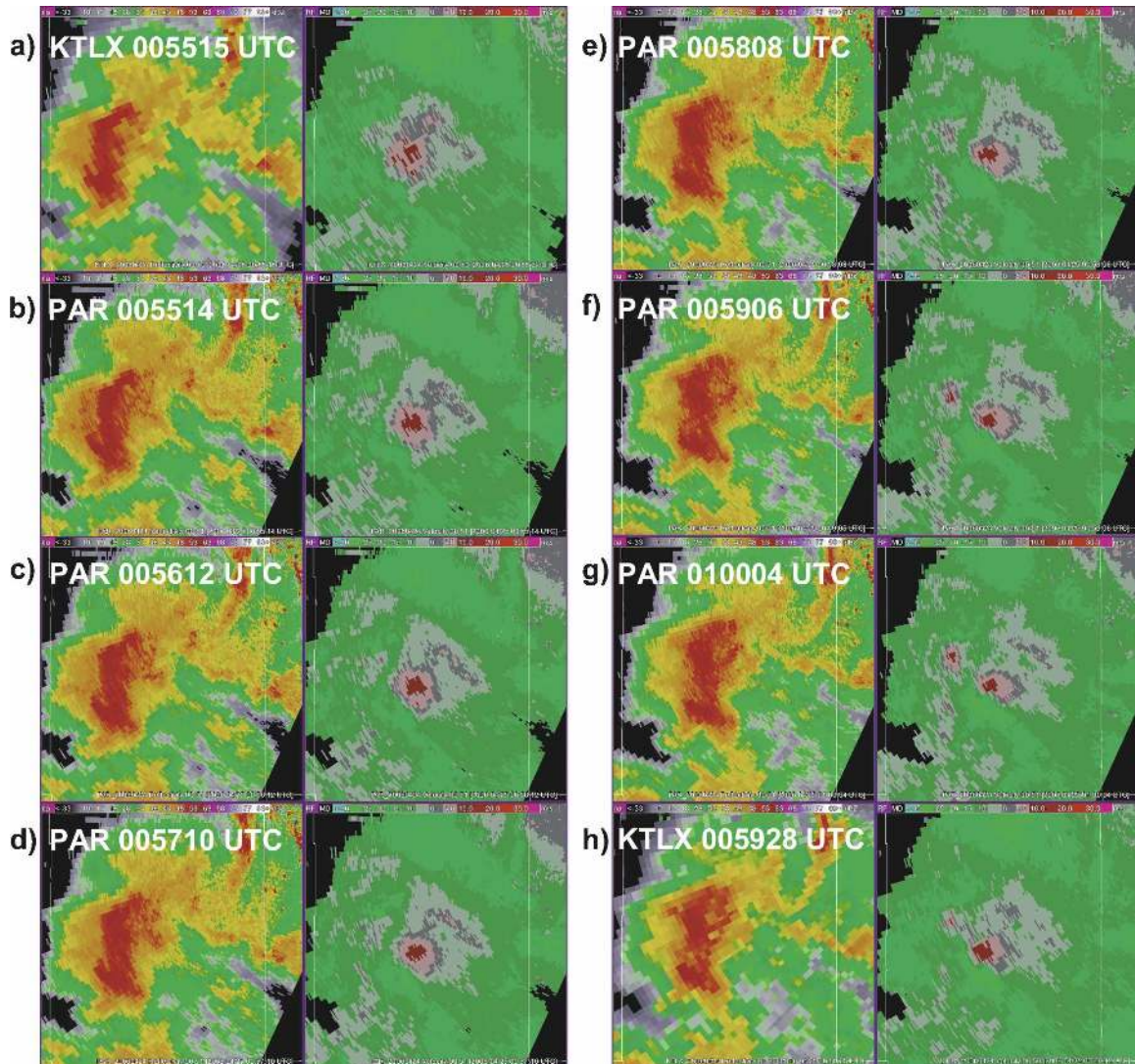


FIG. 2. Development of low-altitude convergence and rotation during a severe thunderstorm near Norge, OK (about 50 km southwest of PAR), on 25 Apr 2006. The top-left and bottom-right panels are consecutive  $0.5^\circ$  elevation scans from KTLX. The panels in between are consecutive  $0.5^\circ$  elevation scans from the PAR. There are 252 s between the KTLX scans and 58 s between the PAR scans. North is located at the top of each image. Note in (b)–(g) the detailed development of the gust front depicted by the increasing inbound (green) velocity to the south-southwest of the outbound (red) velocity and, in (e)–(g), 1) the development of rotation on the southeast side of the convergence zone and 2) the intensification of divergent outflow from the forward-flank downdraft. An annotated version of Fig. 2g is given in Fig. 3.

rivative (LLSD) estimates of the vorticity were computed from the velocity data (Smith and Elmore 2004). The PAR's slightly higher values of LLSD-derived vorticity (Fig. 4) result from differences in the range of the circulation from the respective radars (see Fig. 2 of Smith and Elmore 2004). Data collected from the Radar Operations Center's (ROC) developmental WSR-88D (KCRI), which is also located in Norman and is almost collocated with the PAR, have LLSD-derived vorticity values that more closely match those of the PAR (not shown). Thus, comparisons are weighted to-

ward the *trend* of the vertical profile of the cyclonic vorticity within the storm more so than the magnitude.

The series of images in Fig. 4 show the development and evolution of a cyclonic–anticyclonic (red–blue) velocity couplet in the midlevels of the storm. Note the increasing intensity of the cyclonic rotation (denoted by the darker red areas) at the same altitude between successive PAR volume scans, particularly at the 4.31- and 6.79-km slices. Of greater interest is the descending nature of the cyclonic rotation that the PAR captures. The potential capability to diagnose the evolution of

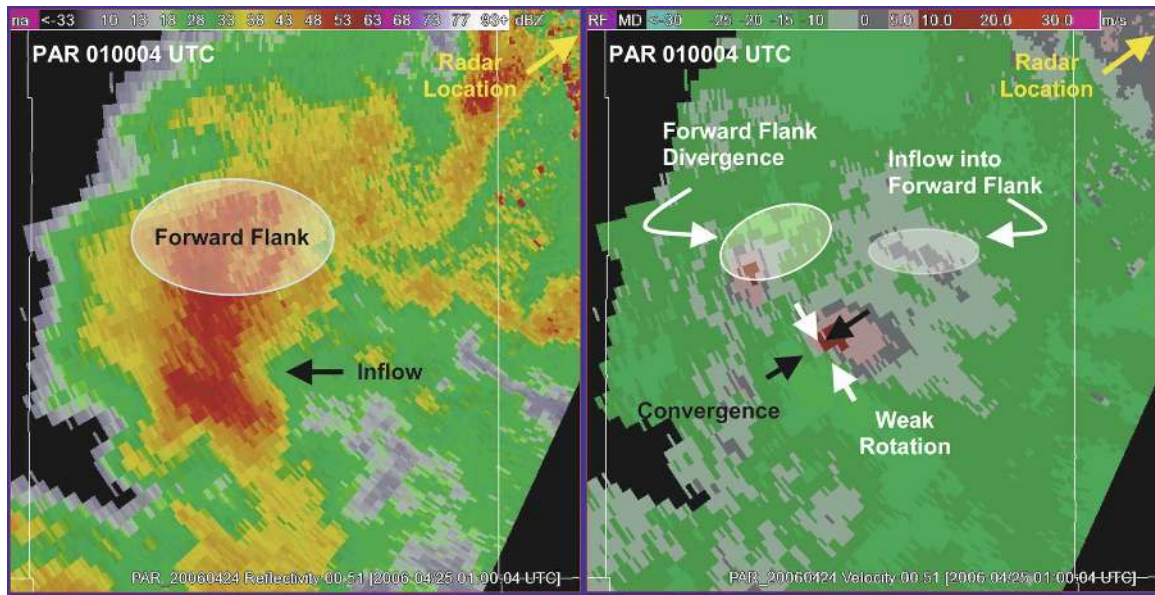


FIG. 3. An annotated view of the velocity signatures present in Fig. 2g.

these velocity signatures may be particularly advantageous in studies of storms exhibiting nondescending vortex development such as those described in Trapp et al. (1999).

#### b. Microburst

During the early evening hours of 10 July 2006, a severe, high-reflectivity (or “wet”) microburst event was observed with the PAR, Oklahoma City TDWR, and KTLX WSR-88D radars. This storm formed within 40 km of the PAR site (Fig. 1) and was sampled with a temporal resolution of approximately 34 s. The atmosphere in central Oklahoma at the time of the event was characterized by moderate surface-based CAPE (2000–2500 J kg<sup>-1</sup>), weak winds aloft, and an elevated dry layer at about 4.5 km MSL. Downdraft convective available potential energy (DCAPE; Gilmore and Wicker 1998), a measure of the atmosphere’s instability to downdrafts, was approximately 1100 J kg<sup>-1</sup>.

Microbursts are small-scale (<4 km diameter) outflows induced by strong downdrafts in thunderstorms that frequently cause damage to property and are a hazard to aviation (Proctor 1988). Many severe microbursts originate from storm cells that form in regions of moderate-to-high CAPE, weak environmental shear, and environments that are highly unstable to downdraft formation. These storm cells typically have a life cycle of 20–40 min, which makes them very difficult to predict or adequately sample temporally with a mechanically steered radar antenna.

Results from the Joint Airport Weather Studies

project suggest that radar-scan update rates for microburst-producing storms should be no greater than 2 min and that several possible “precursors” may be detected aloft prior to the onset of strong outflow (Wilson et al. 1984). These findings have led to the development of automated algorithms that analyze radar data and make short-term predictions for microburst events, as well as detect low-altitude divergence signatures associated with their outflows, for the WSR-88D and TDWR systems (Smith et al. 2004; Wolfson et al. 1994). Precursors used by these algorithms that have been identified in prior studies (Roberts and Wilson 1989; Eilts et al. 1996) include rapidly descending reflectivity cores that oftentimes start at an altitude higher than other storms in the same environment, and strong, deep convergence at middle altitudes of the storm. However, microburst events evolve rapidly, and because the WSR-88D and TDWR typically only sample the upper portions of a storm once every 4–6 min (depending on scanning strategy), they may or may not sample key precursor features aloft. In this case, the PAR scanned an elevated reflectivity core that rapidly descended a few minutes prior to the onset of strong outflow near the surface. The KTLX WSR-88D scanned this storm in VCP 11 with an update rate of 5 min between volume scans, thus missing much of the evolution that was captured by the PAR.

#### 1) PAR SCANNING STRATEGY

Since widespread small convective storms occurred on this day, a 90° sector was chosen to maximize cov-

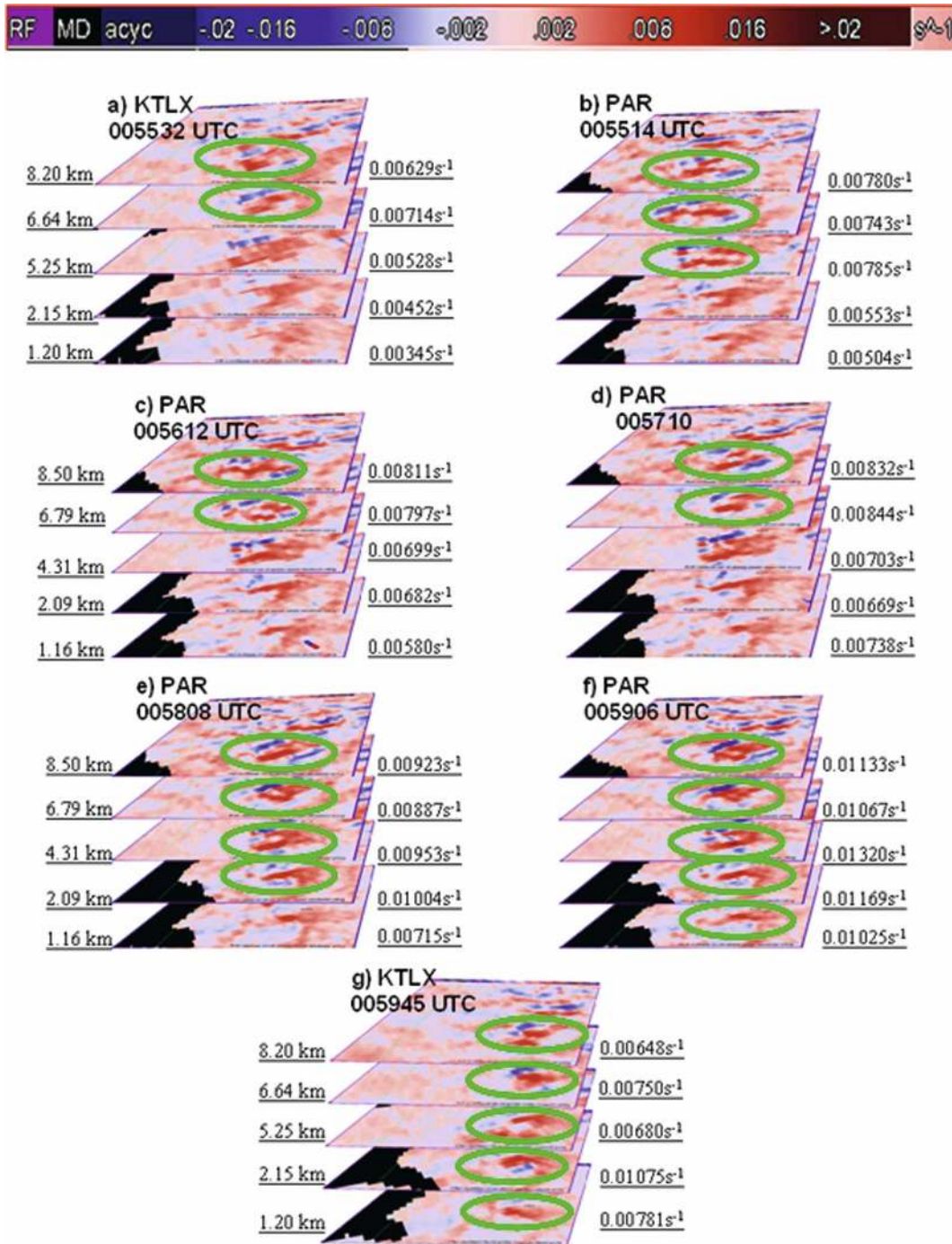


FIG. 4. Selected elevation scans (see Table 2) of the azimuthal shear fields for (a), (g) KTLX and (b)–(f) PAR. The first KTLX velocity scan started at 0055:32 UTC on 25 Apr 2006 and the next KTLX velocity scan started at 0059:45 UTC. Red (blue) areas indicate cyclonic (anticyclonic) vorticity, whereas darker colors indicate more intense rotation. Along the left side of the image each layer is labeled with the approximate altitude above the earth's surface at the center of the layer. The right side of each image is labeled with the maximum cyclonic vorticity for the area of interest. Figs. 2b–f show the same construct but for the PAR. The beginning time for each volume scan is labeled for each image. Note the descending cyclonic vorticity maxima in the PAR images. The green ovals highlight areas where maximum vorticity values exceed arbitrary thresholds of  $0.0075 \text{ s}^{-1}$  (PAR) and  $0.0055 \text{ s}^{-1}$  (KTLX). (The differing thresholds account for the range dependency of the LLS calculations.)

TABLE 2. Description of KTLX and PAR elevation angles and heights above sea level (called “layers” in the text) illustrated in Fig. 4.

KTLX		PAR	
Elevation angle (°)	Height above sea level (km)	Elevation angle (°)	Height above sea level (km)
0.5	1.20	1.3	1.16
1.3	2.15	2.4	2.09
3.1	4.5	5.1	4.31
5.1	6.64	8.0	6.79
6.4	8.20	10.0	8.50

erage. During the analysis period, the phased-array antenna was aimed toward the south-southwest of the radar to collect continuous data on the lines and clusters of small convective storms that developed within the sector. The PAR employed a VCP 12 beam multiplexing scanning strategy, which produced 34-s volume scan updates. Beam multiplexing is different from conventional scanning strategies because data are collected in an interleaved fashion from *multiple* beam positions during the total dwell time. The increased time between pulses at a particular beam position can produce moment data with lower errors compared to conventional contiguous-pulse data collection (Yu et al. 2007).

## 2) ANALYSIS

Several lines and clusters of small convective cells, along with a few embedded stronger cells and numerous interacting outflow boundaries, formed on this day. One storm that produced a strong outflow was located to the south-southwest of all three radars, approximately 15 km from the PAR, 17 km from the TDWR, and 34 km from the WSR-88D (Fig. 1). The PAR detected a new core aloft at 1940:21 UTC, and this cell produced a strong outflow sampled near the surface of  $30 \text{ m s}^{-1}$  at 1956:00 UTC. Although this storm produced radial wind speeds meeting National Weather Service severe criteria, no damage from this event was reported. This storm was fully sampled by the PAR a total of 23 times from the first detection of the core aloft to the outflow time. By way of comparison, the WSR-88D completed only about 3.5 volume scans in the same period of time and did not sample the peak outflow, while the TDWR (not shown) sampled the near-surface outflow once per minute but poorly sampled the three-dimensional evolution of the storm cell.

Figure 5 shows data from the 4 KTLX volume scans and 16 PAR volume scans that illustrate the temporal evolution of the event. Each panel shows the vertical

profile of the reflectivity (left) and the LLSD radial divergence (right; Smith and Elmore 2004). The LLSD radial divergence field is typically very noisy outside of storm regions, but within a storm region it is useful for identifying areas of convergence and divergence. Because the storm is rapidly scanned by the electronically steered PAR beam, the temporal evolution of the entire storm cell is more fully sampled and rapidly changing features are not missed between volume scans.

Between 1940:21 and 1942:20 UTC (Figs. 5b and 5c), a new reflectivity core is developing in intensity aloft at about 6 km above ground level (AGL; hereafter,  $Z$  in the vertical cross section) and 1 km from the left of the image (hereafter,  $X$  in the vertical cross section). Beneath the core at  $X = 2 \text{ km}$ ,  $Z < 0.5 \text{ km}$ , an area of radial convergence (negative radial divergence; blue) indicates convergence at the base of the updraft. To the immediate right, centered on  $X = 4.5 \text{ km}$ , a previous storm cell in the latter half of its life cycle extends to the surface with a small area of weak divergence apparent at its base. An area of divergence is located near the storm top at  $X = 3 \text{ km}$ ,  $Z = 7 \text{ km}$ , but the storm top is not fully sampled by the PAR. The PAR data capture a transient weak echo region at  $X = 3 \text{ km}$ ,  $Z = 5 \text{ km}$  that coincides with the updraft (for about 1 min) and is not sampled by the WSR-88D or TDWR.

During the next 7 min, the core intensifies, elongates, and descends (PAR, Figs. 5d,e and 5g-j; KTLX, Fig. 5f), ultimately producing an initial weak outflow centered at  $X = 7 \text{ km}$ , and a deep layer of convergence aligned with the highest reflectivity values located aloft (PAR, Fig. 5l; cf. to KTLX, Fig. 5k, between  $Z = 1 \text{ km}$  and  $Z = 6 \text{ km}$ ). Owing to the less frequent scanning of the WSR-88D, KTLX does not sample these evolving microburst precursors. During the next 2 min, although the updraft is beginning to dissipate, the high-reflectivity core and strong, deep convergence are maintained (Figs. 5m-o). About 3 min thereafter (1956:00 UTC), a very strong gust ( $30 \text{ m s}^{-1}$ ) is indicated in the radial velocity field (not shown) as the storm moves closer to the radar and decays (KTLX, Fig. 5p; PAR, Figs. 5q-s). The shallow outflow is not as apparent in the KTLX data as in the PAR and TDWR data, partially because the beam was higher above the surface at the longer range (34 km from KTLX versus 15 km from PAR), but also because the maximum velocity measurement occurs temporally between KTLX low-altitude elevation scans. By 1958:07 UTC (Fig. 5t), the PAR is still sampling strong outflow from the storm cell, and a “precipitation foot”—precipitation that



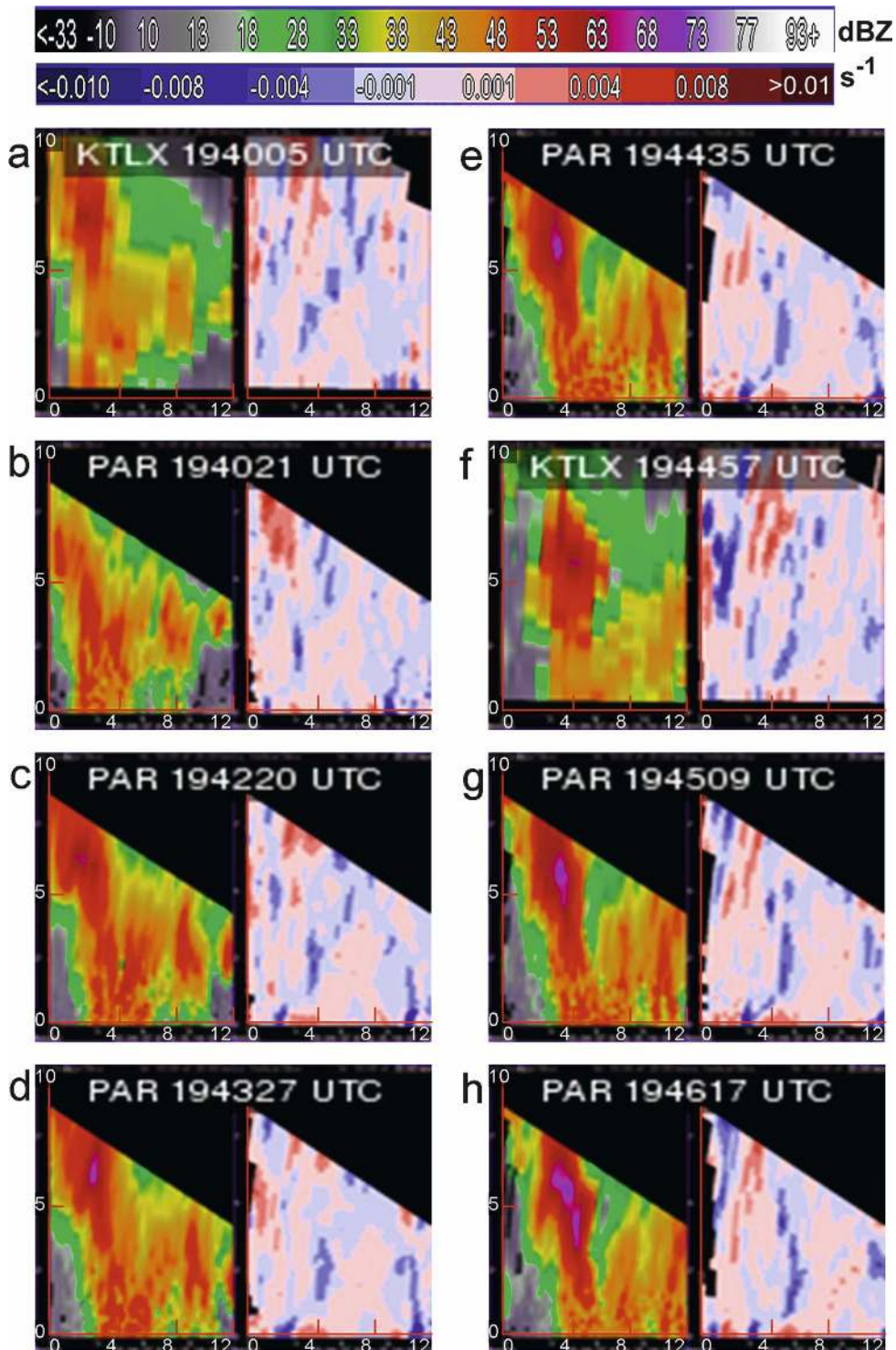


FIG. 5. A time series of PAR and KTLX WSR-88D data showing the evolution of a strong microburst event on 10 Jul 2006. Each panel shows the vertical cross section of the reflectivity (dBZ; left) and LLS radial divergence ( $s^{-1}$ ; right) taken along the 12-km-long line shown in Fig. 1. Increasing distance along the horizontal axis corresponds to decreasing distance from the PAR ( $X = 0$  is approximately 20 km in range from the PAR). Both the horizontal and vertical axes are given in km. The reflectivity (left) and radial divergence (right) color scales are shown at the top of the figure. The time stamps shown are for the beginning of each volume scan. Although the storm was sampled completely every 34 s, for brevity, every other cross section is displayed at  $\sim 1$  min intervals.

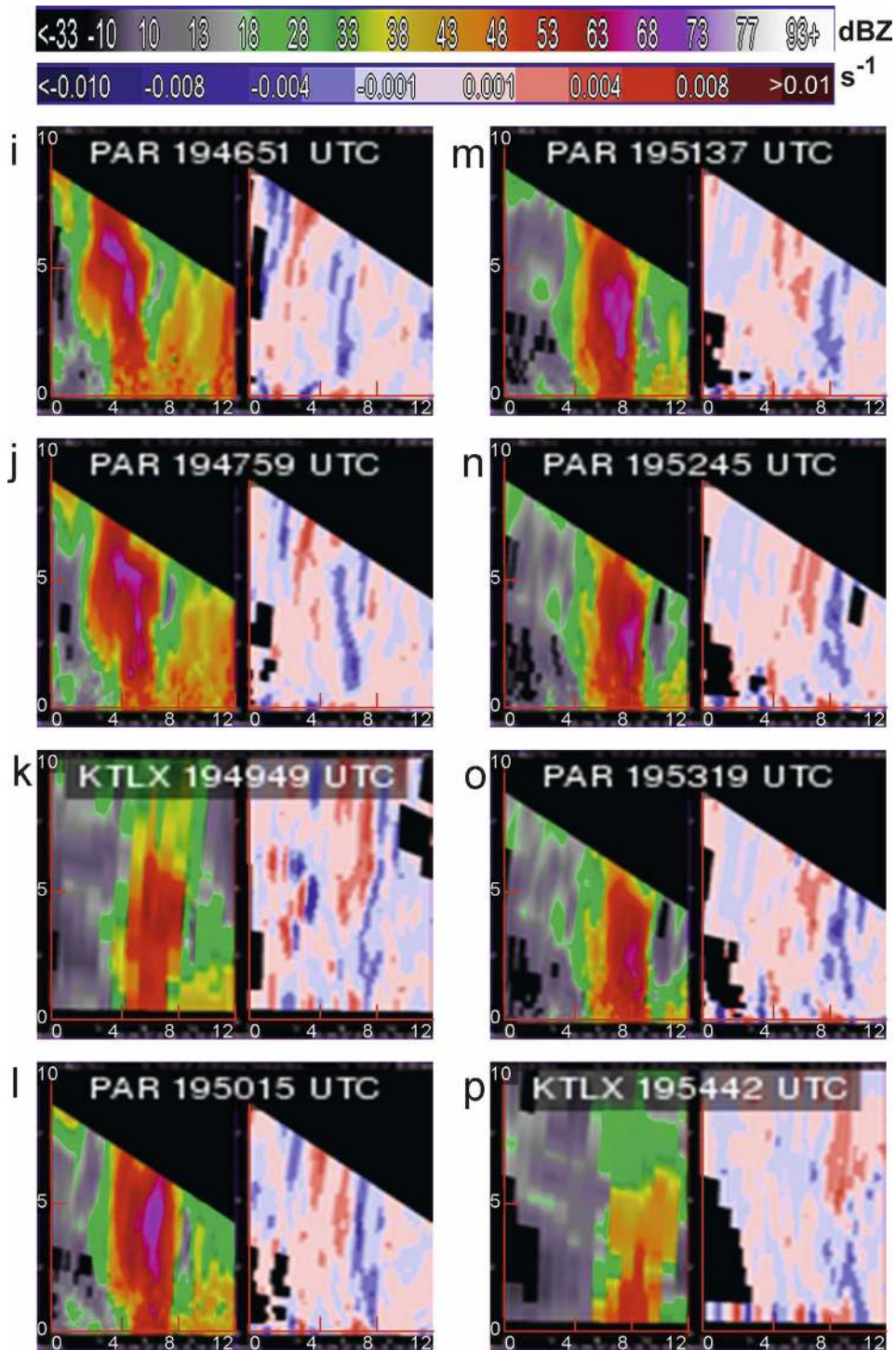


FIG. 5. (Continued)

is carried horizontally outward from the cell with a strong outflow near the surface—is visible in the reflectivity field to the left of the main reflectivity core at  $X = 8\text{--}10$  km,  $Z = 1$  km. We strongly suspect that the

illustrated high-resolution sampling of microburst precursors will support the development of prediction algorithms with higher accuracy than convective radars.

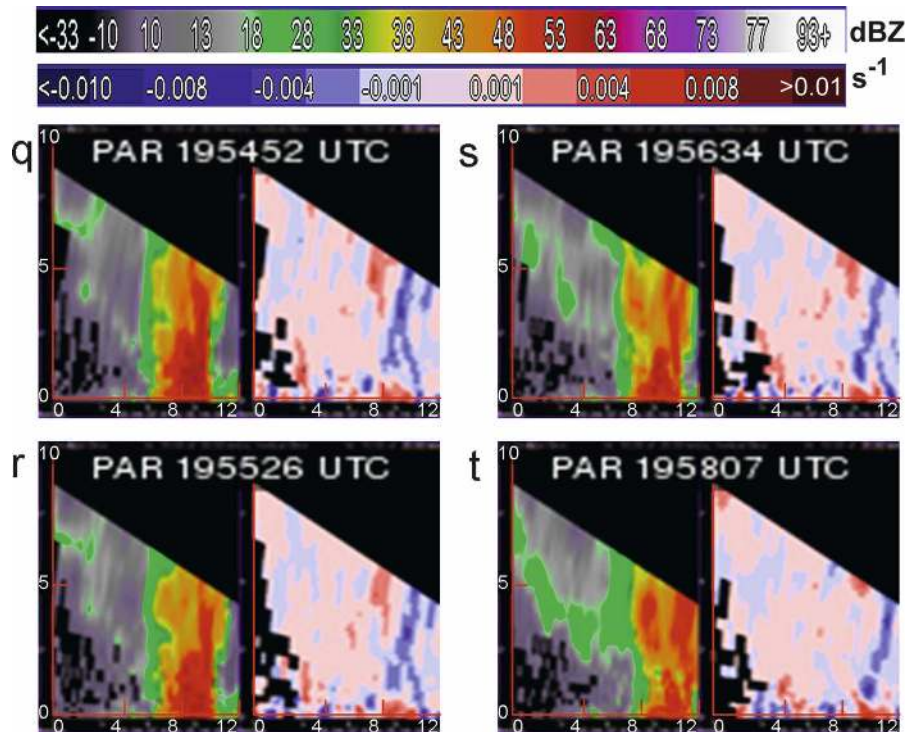


FIG. 5. (Continued)

### c. Hailstorm

The atmospheric environment across central Oklahoma on 15 August 2006 consisted of a moist-unstable air mass, capped by an inversion near 7.8 km (MSL). The vertical wind shear was weak with predominantly south-southwesterly winds below the inversion and northeasterly winds above the inversion. During the day, increasing surface-based CAPE values [362  $J\ kg^{-1}$  (1200 UTC 15 August) to 822  $J\ kg^{-1}$  (0000 UTC 16 August) at the Norman, Oklahoma, sounding site] and negative lifted indices ( $-2.2^{\circ}$  to  $-3.5^{\circ}C$ ) indicated that the atmosphere became more unstable.

In the early afternoon, surface temperatures in south-central Oklahoma climbed into the mid 30s ( $^{\circ}C$ ) while dewpoint temperatures reached  $20^{\circ}C$ . Deep convection began south of Norman in the form of isolated storms, with life spans on the order of 30–40 min and maximum reflectivity values between 50 and 60 dBZ. Maximum echo-top heights (based on a 20-dBZ threshold) were generally 8 km (MSL) or lower, coinciding with the height of the midaltitude capping inversion. After 2222 UTC, a storm approximately 40 km to the west-southwest of the PAR quickly broke through the capping inversion (Fig. 1). Using a volume scan sampling rate of 26 s, the entire evolution of the storm was captured. In particular, the PAR data depicted the evolution of a three-body scatter spike (TBSS) artifact as-

sociated with a developing hail region aloft in more detail than in previous studies (Zrnić 1987; Wilson and Reum 1988; Nielsen-Gammon and Read 1995; Lemon 1998; Brown and Torgerson 2003). Although KTLX WSR-88D data were unavailable during this event, the information presented here is used to consider the gaps in the storm life cycle resulting from a typical VCP 11 scanning strategy ( $\sim 5$  min updates).

#### 1) PAR SCANNING STRATEGY

One of the goals for data collection on 15 August was to capture the evolution of a severe storm in more detail than is currently possible with the WSR-88D, both spatially and temporally. Based on characteristics in the 1200 UTC Norman, Oklahoma, sounding, storms breaking the capping inversion were expected to grow in excess of 12 km in height. In a traditional WSR-88D precipitation-mode VCP, the upper elevation angle of  $19.5^{\circ}$  would not sample storm tops with heights 12 km or taller inside of a 35-km range. Moreover, the spacing between elevation angles above  $6^{\circ}$  undersamples the vertical structure of storms. To improve the vertical sampling, a scanning strategy was chosen that contained 31 elevation angles, ranging from  $0.5^{\circ}$  to  $41^{\circ}$  with elevation angles mimicking VCP 12 below  $6^{\circ}$  and a maximum spacing of  $1.5^{\circ}$  above  $6^{\circ}$ . Also, to keep the volume scan time under 30 s, each elevation angle used

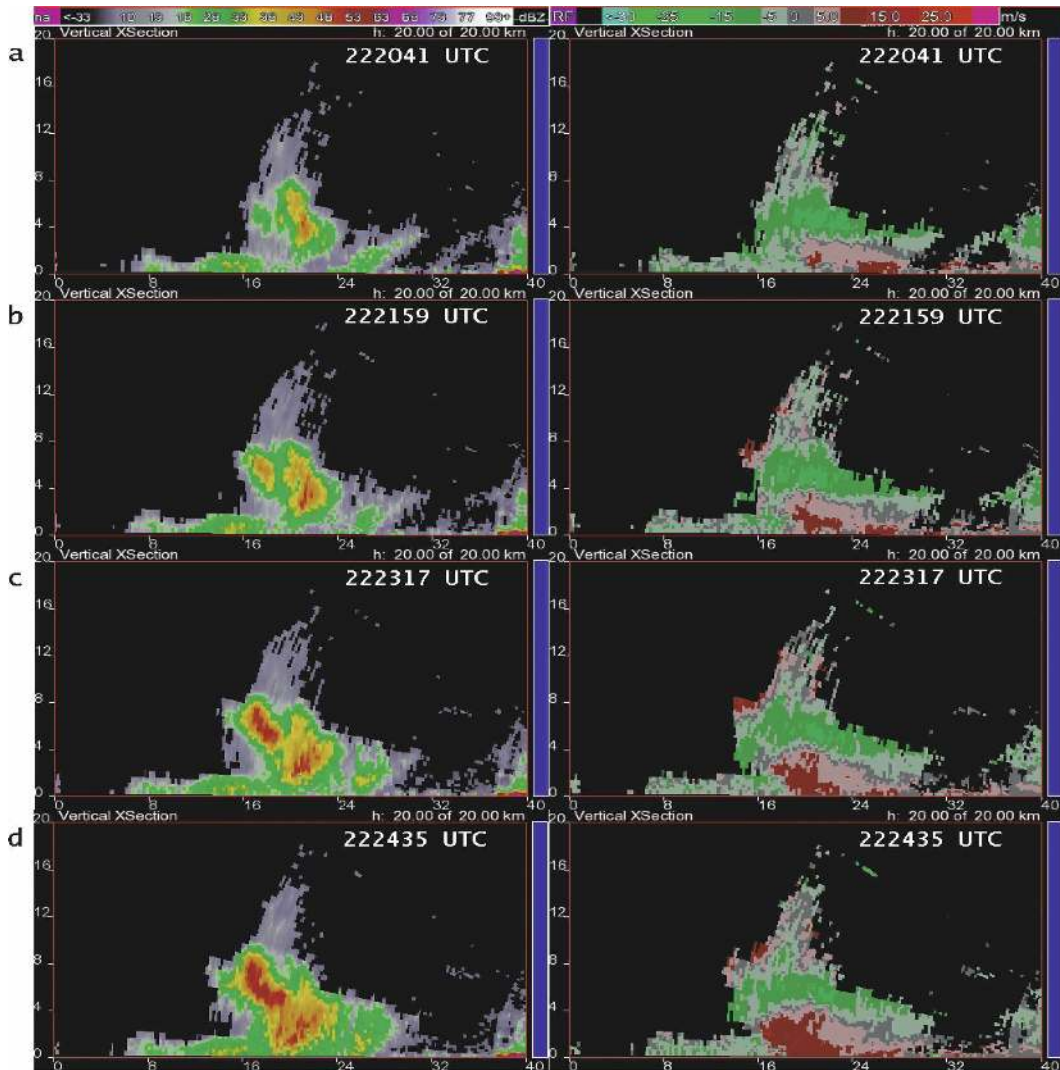


FIG. 6. Time series of PAR data showing the evolution of a hailstorm on 15 Aug 2006. Each panel shows the vertical cross section of reflectivity (dbZ; left) and radial velocity ( $\text{m s}^{-1}$ ; right) taken along the 40-km-long line shown in Fig. 1. Increasing distance along the horizontal axis corresponds to decreasing distance from the PAR ( $X = 0$  is approximately 50 km in range from the PAR). Both the horizontal and vertical axes are given in km. The reflectivity (left) and radial velocity (right) color scales are shown at the top of the figure. The time stamps shown are for the beginning of each volume scan. Although the storm was sampled completely every 26 s, for brevity, every third cross section is displayed at  $\sim 78$  s intervals.

a pulse repetition time (PRT) of  $831 \mu\text{s}$  with 12 pulses per dwell. Although reducing the number of pulses per dwell diminished the accuracy of the radial velocity estimates from traditional WSR-88D scans, the errors were still within  $\pm 2 \text{ m s}^{-1}$ . Additionally, the short PRT increased the chances for detecting second-trip echoes in the lowest elevation cuts.

## 2) ANALYSIS

This section describes the life cycle of the hailstorm (Fig. 6). Even though no hail was reported in the vicin-

ity of this storm, the classic radar reflectivity hail signatures produced by the storm suggest that hail likely reached the ground in the low-population area where the storm occurred. Although the storm was sampled completely every 26 s, for brevity, every third cross section is displayed ( $\sim 78$  s intervals). The first 20 min (most active part) of the storm life cycle is presented in  $\sim 5$  min segments to approximate and compare the evolution observable by a WSR-88D running a VCP 11 scanning strategy (Fig. 6). In this analysis, all storm-top references assume a 20-dBZ threshold.

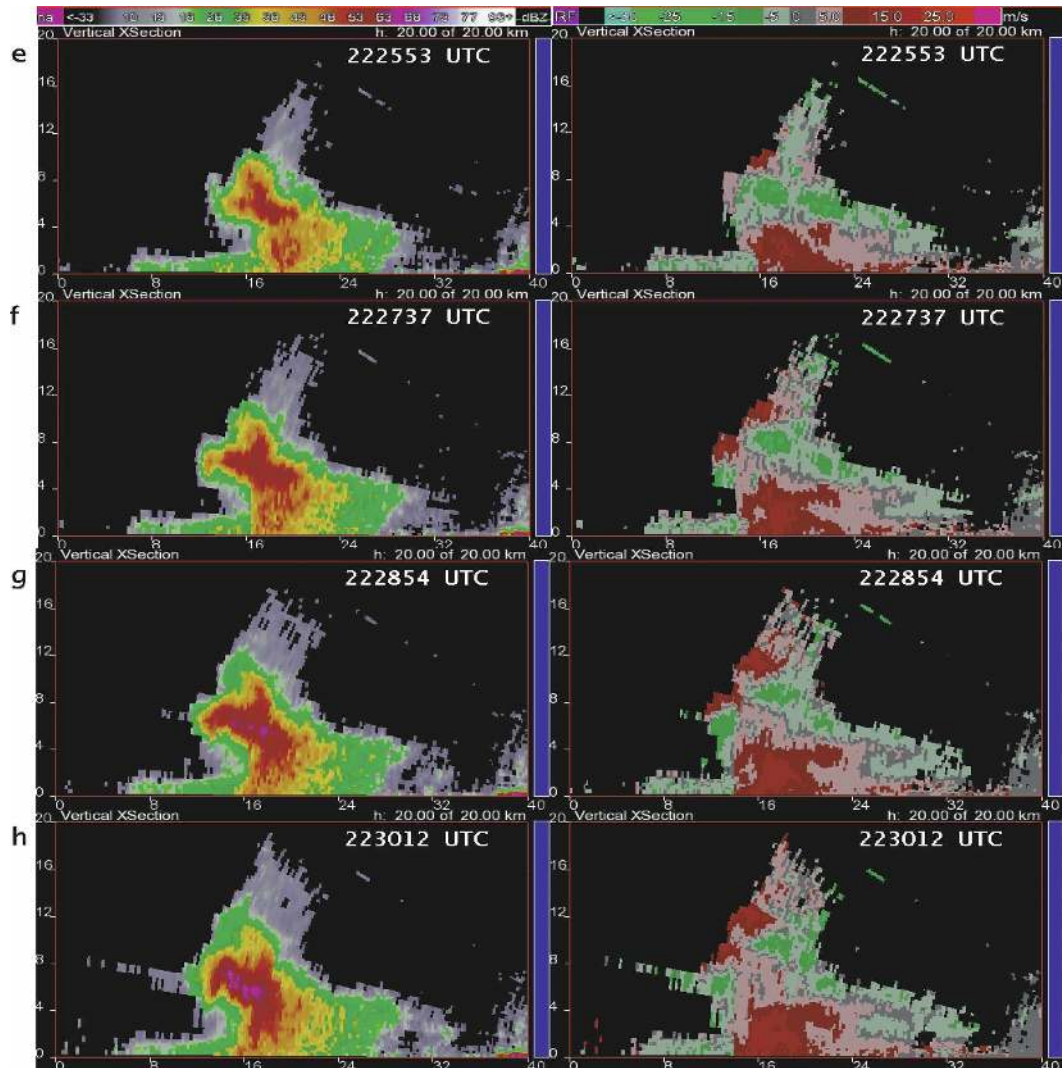


FIG. 6. (Continued)

During the period of one VCP 11 scan (2220:41–2224:35 UTC; Figs. 6a–d), the storm-top height (centered at  $X = 17$  km,  $Z = 5$  km) quickly grows from 5 to 9 km (AGL) and the maximum reflectivity values increase from  $\sim 30$  to  $\sim 55$  dBZ. This increase in maximum reflectivity values occurs while the inflow region to the right of the developing storm deepens ( $X = 16$ – $24$  km,  $Z = 0$ – $4$  km) and increases in area (area of radial velocities over  $10 \text{ m s}^{-1}$  grows from under  $1 \text{ km}^2$  to over  $20 \text{ km}^2$ ). The updraft supporting this rapid growth is indicated by the near-surface radial convergence below the high-reflectivity core and the radial divergence aloft. The weak flare echo ( $< 20$  dBZ) that extends above the storm-top height and increases in height throughout the storm life cycle is a direct result of scattering by sidelobes (Doviak and Zrnić 1993). Features to the left of the core near the surface are

masked by the second-trip echo from a distant storm. Above the second-trip echo, contamination through sidelobes is evident.

A bounded weak echo region (BWER), indicative of an intensifying and deepening updraft ( $X = 13$ – $16$  km,  $Z = 5$ – $7$  km), develops rapidly during the next conventional scan (2225:53–2230:12 UTC; Figs. 6e–h). Further evidence of the deepening updraft is the corresponding development of an area of low-to-midaltitude convergence coincident with the BWER. Meanwhile, the maximum reflectivities above the BWER increase from 55 to near 70 dBZ by 2228:54 UTC (centered at  $X = 16$  km,  $Z = 6$  km), at which time a TBSS is beginning to become visible to the left of the reflectivity core (down range from the PAR), indicating the presence of hail at midaltitudes ( $Z = 7$ – $8$  km).

The high-reflectivity hail core deepens and produces

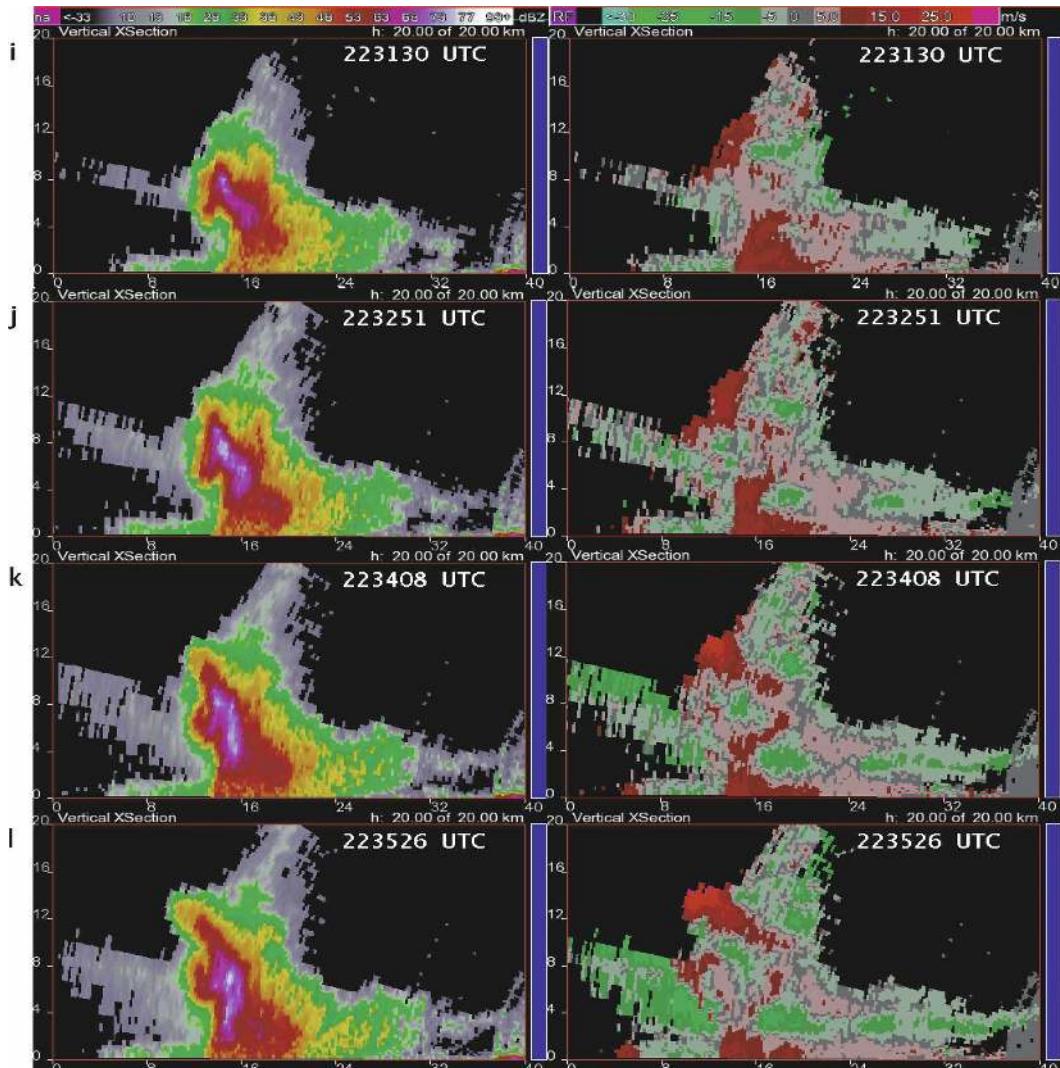


FIG. 6. (Continued)

a better-defined TBSS during the next conventional scan (2231:30–2235:26 UTC; Figs. 6i–l). The deepening of the core is indicated by an increase in maximum reflectivities (up to 75 dBZ) and a change in its shape and orientation. In the 1-min period before 2232:51 UTC (Figs. 6i and 6j), a region of inbound (negative) radial velocities quickly develops on the inflow side of the storm (centered at  $X = 19$  km,  $Z = 4$  km), reducing the depth of the inflow region to the lowest 2 km. In the same 1-min period, the base of the right-side reflectivity core begins to descend and split off from the high-reflectivity core located at the top of the updraft ( $X = 14$  km,  $Z = 8$  km). These changes in the velocity and reflectivity fields indicate the descent of large hydrometeors on the inflow side of the updraft core. In response to the expanding hail region, the length and vertical extent of the TBSS increases. In fact, two

separate TBSS features are discernible in response to the splitting of the reflectivity core (Figs. 6m and 6n).

Although initially obscured by second-trip echo near the surface to the left of the storm, the leading edge of a gust front becomes visible in the velocity data at 2232:51 UTC ( $X = 4$  km) and becomes more evident between 2232:51 and 2235:26 UTC as it propagates westward at about  $10 \text{ m s}^{-1}$  (Figs. 6j–l). During this period, the base of the right-side reflectivity hail core reaches the surface. The descent of this high-reflectivity hail core corresponds with the expansion of the region of low-altitude divergence ( $X = 16$ – $20$  km,  $Z = 2$ – $5$  km) and the dissipation of the BWER.

The top of the storm develops a classic anvil shape that is illustrated by the expansion of both the storm's reflectivity and the region of radial divergence above 8 km during the last examined conventional scan

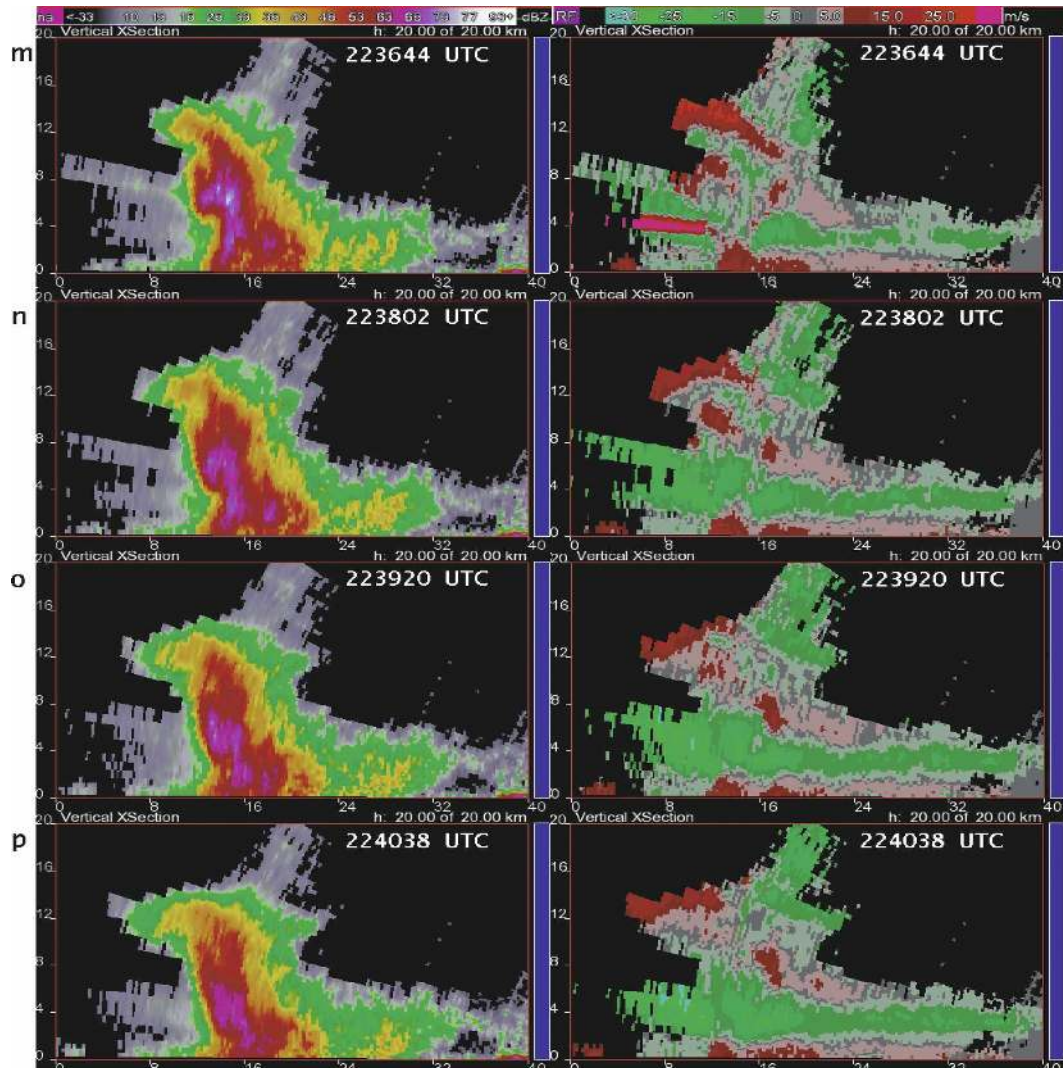


FIG. 6. (Continued)

(2236:44–2240:38 UTC; Figs. 6m–p). Within this period, the anvil expands in the  $x$  direction from 12 to 16 km and storm-top height increases to a maximum of 15 km. As the main updraft weakens, the remaining reflectivity core descends and weakens as well. The radial length and height of its associated TBSS also decrease, which is consistent with previous studies (Zrnić 1987; Wilson and Reum 1988; Brown and Torgerson 2003). The gust front to the left of the storm is still well defined as it propagates to the west. Maximum radial velocities in the gust front (from  $X = 4$  km at 2236:44 UTC to  $X = 1$  km at 2240:38 UTC) are  $\sim 13 \text{ m s}^{-1}$  during this period.

#### 4. Summary

This study demonstrates the NWRT PAR's capability for adaptable, high temporal resolution scanning of

quickly developing features in deep convective storms. Scientific advantages of the PAR's high temporal sampling capability compared to the WSR-88D were examined for three convective storms that occurred during the spring and summer of 2006, including a reintensifying supercell, a microburst, and a hailstorm. The comparative analysis shows that volumetrically sampling these storms at intervals of 58 s or less provides superior depictions of the evolution of the reflectivity and velocity features. Detailed analyses of the three storms revealed the following scientific findings:

- *Reintensifying supercell*—Greater ability to analyze the evolution of quasi-horizontal velocity signatures, including storm inflow, low-altitude intensifying and contracting convergence, and developing cyclonic rotation and forward-flank outflows (divergence); en-

hanced capacity to investigate developments of velocity signatures in the vertical, such as intensifying and descending vorticity maxima within the storm. (Recall that the trends summarized above occurred between two WSR-88D VCP 12 scans, i.e., 4-min period.)

- *Microburst*—Superior ability to analyze the dynamics of a rapidly evolving microburst, including the initial intense updraft, rapidly descending high-reflectivity core, coincident deep, strong midaltitude convergence, and divergence near the ground, which are much more difficult to analyze with 4–6-min WSR-88D scans.
- *Hailstorm*—Enhanced ability to analyze hail threat within a rapidly developing storm, including the development of the BWER about 3 min after the main updraft broke through the capping inversion, and the occurrence of the high-reflectivity core and TBSS artifact another 3 min thereafter.

Although WSR-88D data and operational products are indispensable for assessing storm severity, findings from this paper support the possibility for PARs to provide the high temporal resolution data needed to facilitate earlier detection of significant storm development, convergence, microburst precursors, wind shear, and hail signatures. Forecasters who participated in a preliminary real-time demonstration of the PAR in spring 2007 indicated that rapid-update radar data have the potential to heighten forecaster confidence in the timing, location, and intensity of radar features and trends thereof. An important next step, then, is the production and validation of data quality and severe weather detection algorithms that take advantage of high temporal resolution PAR data. Because users may be challenged by the rapid influx of data, much effort also needs to be expended into research and development to facilitate more automated decision making than current techniques. Another important step is the design and production of a dual-polarized (dual-pol) PAR, and ultimately, a prototype multifunction, dual-pol PAR that matches or exceeds current operational standards (Weber et al. 2007; Zrnić et al. 2007). These research advances will help to quantify the advantages of PAR to the user community.

*Acknowledgments.* Funding was provided by the NOAA/Office of Oceanic and Atmospheric Research under NOAA–University of Oklahoma Cooperative Agreement NA17RJ1227, U.S. Department of Commerce (DOC). The statements, findings, conclusions, and recommendations are those of the authors and do not necessarily reflect the views of NOAA or the U.S.

DOC. We especially thank the leadership of Doug Forsyth and the work of Mark Benner, Dan Suppes, Kurt Hondl, and John Thompson, who kept data collection, archiving, and data display going. We also thank Chris Curtis and Sebastian Torres for sharing their radar engineering expertise; Dick Doviak, Dusan Zrnić, and Rodger Brown for their thoughtful reviews; and the anonymous reviewers for insights that helped to improve the paper.

#### REFERENCES

- Brown, R. A., and K. L. Torgerson, 2003: Interpretation of single-Doppler radar signatures in a V-shaped hailstorm: Part 1—Evolution of reflectivity-based features. *Natl. Wea. Dig.*, **27** (2), 3–14.
- , R. M. Steadham, B. A. Flickinger, R. R. Lee, D. Sirmans, and V. T. Wood, 2005: New WSR-88D volume coverage pattern 12: Results of field tests. *Wea. Forecasting*, **20**, 385–393.
- Burgess, D. W., 2004: High resolution analyses of the 8 May 2003 Oklahoma City storm, Part I: Storm structure and evolution from radar data. Preprints, *22nd Conf. on Severe Local Storms*, Hyannis, MA, Amer. Meteor. Soc., 12.4. [Available online at <http://ams.confex.com/ams/pdfpapers/81939.pdf>.]
- , and M. A. Magsig, 1993: Evolution of the Red Rock, Oklahoma supercell of April 26, 1991. Preprints, *17th Conf. on Severe Local Storms*, St. Louis, MO, Amer. Meteor. Soc., 257–261.
- , and —, 1998: Recent observations of tornado development at near range to WSR-88D radars. Preprints, *19th Conf. on Severe Local Storms*, Minneapolis, MN, Amer. Meteor. Soc., 756–759.
- Doviak, R. J., and D. S. Zrnić, 1993: *Doppler Radar and Weather Observations*. Academic Press, 562 pp.
- Eilts, M. D., J. T. Johnson, E. D. Mitchell, R. J. Lynn, P. Spencer, S. Cobb, and T. M. Smith, 1996: Damaging downburst prediction and detection algorithm for the WSR-88D. Preprints, *18th Conf. on Severe Local Storms*, San Francisco, CA, Amer. Meteor. Soc., 541–545.
- Gilmore, M. S., and L. J. Wicker, 1998: The influence of midtropospheric dryness on supercell morphology and evolution. *Mon. Wea. Rev.*, **126**, 943–958.
- Lemon, L. R., 1998: The radar “three-body scatter spike”: An operational large-hail signature. *Wea. Forecasting*, **13**, 327–340.
- Nielsen-Gammon, J. W., and W. L. Read, 1995: Detection and interpretation of left-moving severe thunderstorms using the WSR-88D: A case study. *Wea. Forecasting*, **10**, 127–140.
- Proctor, F. H., 1988: Numerical simulations of an isolated microburst. Part I: Dynamics and structure. *J. Atmos. Sci.*, **45**, 3137–3160.
- Roberts, R. D., and J. W. Wilson, 1989: A proposed microburst nowcasting procedure using single-Doppler radar. *J. Appl. Meteor.*, **28**, 285–303.
- ROC, 2007: WSR-88D system specification. WSR-88D Radar Operations Center Rep. OWY55, 164 pp. [Available from NOAA FOIA Office, Public Reference Facility (OFA56), 1315 East West Hwy. (SSMC3), Room 10730, Silver Spring, MD 20910.]
- Smith, T. M., and K. L. Elmore, 2004: The use of radial velocity derivatives to diagnose rotation and divergence. Preprints,



- 11th Conf. on Aviation, Range, and Aerospace*, Hyannis, MA, Amer. Meteor. Soc., P5.6. [Available online at <http://ams.confex.com/ams/pdfpapers/81827.pdf>.]
- , —, and S. A. Dulin, 2004: A damaging downburst prediction and detection algorithm for the WSR-88D. *Wea. Forecasting*, **19**, 240–250.
- Trapp, R. J., E. D. Mitchell, G. A. Tipton, D. W. Effertz, A. I. Watson, D. L. Andra Jr., and M. A. Magsig, 1999: Descending and nondescending tornadic vortex signatures detected by WSR-88Ds. *Wea. Forecasting*, **14**, 625–639.
- Weber, M. E., J. Y. N. Cho, J. S. Herd, J. M. Flavin, W. E. Benner, and G. S. Torok, 2007: The next-generation multimission U.S. surveillance radar network. *Bull. Amer. Meteor. Soc.*, **88**, 1739–1751.
- Wilson, J. W., and D. Reum, 1988: The flare echo: Reflectivity and velocity signature. *J. Atmos. Oceanic Technol.*, **5**, 197–205.
- , R. D. Roberts, C. Kessinger, and J. McCarthy, 1984: Microburst wind structure and evaluation of Doppler radar for airport wind shear detection. *J. Climate Appl. Meteor.*, **23**, 898–915.
- Wolfson, M. M., R. L. Delanoy, B. E. Forman, R. G. Hallowell, M. L. Pawlak, and P. D. Smith, 1994: Automated microburst wind-shear prediction. *Lincoln Laboratory Journal*, Vol. 7, MIT Lincoln Laboratory, 399–426.
- Yu, T.-Y., M. B. Orescanin, C. D. Curtis, D. S. Zrnić, and D. E. Forsyth, 2007: Beam multiplexing using the phased-array weather radar. *J. Atmos. Oceanic Technol.*, **24**, 616–626.
- Zhang, G., and R. J. Doviak, 2007: Spaced-antenna interferometry to measure crossbeam wind, shear, and turbulence: Theory and formulation. *J. Atmos. Oceanic Technol.*, **24**, 791–805.
- Zrnić, D. S., 1987: Three-body scattering produces precipitation signature of special diagnostic value. *Radio Sci.*, **22**, 76–86.
- , and Coauthors, 2007: Agile-beam phased array radar for weather observations. *Bull. Amer. Meteor. Soc.*, **88**, 1753–1766.